

Langevin dynamics of the two-stage melting transition of vortex matter in $\text{Bi}_2\text{Sr}_2\text{CaCu}_2\text{O}_{8+\delta}$ in the presence of straight or tilted columnar defects

Yadin Y. Goldschmidt and Jin-Tao Liu

Department of Physics and Astronomy, University of Pittsburgh, Pittsburgh, Pennsylvania 15260, USA

(Received 21 March 2007; revised manuscript received 6 July 2007; published 13 November 2007)

In this paper, we use London-Langevin molecular dynamics simulations to investigate the vortex matter melting transition in the highly anisotropic high-temperature superconductor material $\text{Bi}_2\text{Sr}_2\text{CaCu}_2\text{O}_{8+\delta}$ in the presence of low concentration of columnar defects (CDs). We reproduce with further details our previous results obtained by using multilevel Monte Carlo simulations that showed that the melting of the nanocrystalline vortex matter occurs in two stages: a first stage melting into nanoliquid vortex matter and a second stage delocalization transition into a homogeneous liquid. Furthermore, we report on dynamical measurements in the presence of a current that clearly identifies the irreversibility line and the second stage delocalization transition. In addition to CDs aligned along the c axis, we also simulate the case of tilted CDs which are aligned at an angle with respect to the applied magnetic field. Results for CDs tilted by 45° with respect to the c axis show that the locations of the melting and delocalization transitions are not affected by the tilt when the ratio of flux lines to CDs remains constant. On the other hand, we argue that some dynamical properties and, in particular, the position of the irreversibility line, should be affected.

DOI: [10.1103/PhysRevB.76.174508](https://doi.org/10.1103/PhysRevB.76.174508)

PACS number(s): 74.25.Qt, 74.25.Ha, 74.25.Dw, 74.25.Bt

I. INTRODUCTION

Since their discovery during the 1980s, much progress has been made on the study of high-temperature superconductors. These materials are classified as type II superconductors, for which there is only a partial Meissner effect when the external magnetic field is in the range $H_{c1} < H < H_{c2}$.^{1–3} Inside the superconductors, the magnetic field survives in the form of quantized flux lines (FLs), called vortices, each with a quantum unit of flux $\phi_0 = hc/2e$. The vortices form a periodic hexagonal lattice (Abrikosov lattice) at low temperatures and melt into a vortex liquid at higher temperatures.^{4–9}

High-temperature superconductors are ceramic materials which have the common structure of layered superconducting copper-oxide planes. They are anisotropic materials, with anisotropy defined as $\gamma = \sqrt{m_z/m_\perp}$, where m_z and m_\perp are the effective masses of electrons moving perpendicular to the superconducting planes and along them, respectively. One of the commonly studied materials $\text{Bi}_2\text{Sr}_2\text{CaCu}_2\text{O}_{8+\delta}$, known as BSCCO, is highly anisotropic. It is estimated to have an anisotropy in the range of 300–500 for optimally doped samples.

In high anisotropic materials, vortices can be described as stacks of pancake vortices.^{10,11} The “pancakes” are centered at their corresponding planes and can only move within their own planes. The interaction between the pancakes consists of two parts: the electromagnetic interaction and the Josephson interaction.

The electromagnetic interaction originates from the screening currents that arise in the same plane where a pancake resides, as well as in more distant planes. It is repulsive among pancakes in the same plane and attractive for those in different planes.^{10,12} This interaction exists even in the case where the superconducting planes are completely decoupled, so no current can flow along the c axis (perpendicular to the planes) of the sample.

The Josephson interaction^{2,12,13} originates from the Josephson current flowing between the superconducting planes,

which is proportional to the sine of the gauge invariant phase difference between two planes $\Delta\varphi + (2\pi/\phi_0) \int ds \cdot \mathbf{A}$, where φ is the phase of the superconducting order parameter and \mathbf{A} is the vector potential. When two pancakes belonging to the same stack and residing in adjacent planes move away from each other, the phase difference that originates causes a Josephson current to begin flowing between the planes. This results in an attractive interaction between pancakes that for distances small compared to $\Lambda \equiv \gamma d$ is approximately quadratic^{2,12} in the distance. Here, we denoted by d the interplane separation. When the two adjacent pancakes are separated by a distance larger than Λ , a “Josephson string” is formed, whose energy is proportional to its length.^{13,14}

Recently, the effect of columnar defects (CDs) on the melting transition was investigated both experimentally^{15–17} and numerically.^{18–21} Columnar defects can be induced artificially by irradiating the sample with high energy heavy ions, such as 1 GeV lead ions. The heat released by the ions creates tubes of damaged, nonconducting material. It is customary to measure the density of CDs by the value of the “matching field” by $B_\phi = n_{cd}\phi_0$, where n_{cd} is the number of CDs per unit area. In the limit $B \ll B_\phi$, the vortex solid becomes a Bose glass as most FLs are trapped by CDs located at random positions.^{2,22–24} On the other hand, our interest is in the case $B_\phi \leq B$, in which there are more FLs than CDs. In this case, the picture that emerged from experiments,^{15–17} from numerical investigations,^{18–21} and from analytical calculations^{21,25} is that of the “crystallites in the pores,” also referred to as the “porous” vortex solid. At low temperatures, a skeleton (or matrix) of vortices localized on CDs is formed, while the excess (interstitial) FLs try to form hexagonal crystallites in the lacuna between CDs. Thus, this phase has a short ranged translational order, which extends to a distance of the order of a typical pore size.

As the temperature is increased, and if the magnetic field is large enough, this heterogeneous structure melts in two stages: first, the crystallites in the pores melt into a nanoliq-

uid while the skeleton remains intact, and subsequently, the skeleton melts and the liquid becomes homogeneous. When the magnetic field is lowered, these two transitions coincide into one. This is usually associated with a kink in the first-order melting line. The first stage melting of the crystallites is observed in the experiments as a step in the equilibrium local magnetization^{7,8,26} and in the simulations as a sharp increase in the transverse fluctuations of the FLs, among other signatures. The second transition was not observed in the experiments as a similar jump in the magnetization or another equilibrium property. It was observed in transport measurement¹⁷ involving transport currents with alternating polarity. This establishes the transition as dynamical in nature. It remains to be established that this is also an equilibrium thermodynamic transition. In order to support this assertion, it was argued¹⁷ that the second “delocalization” transition is associated with the restoration of a broken longitudinal gauge symmetry. However, at this time, it cannot be ruled out that the second transition is only a crossover associated with a gradual equilibrium change over a finite range of temperatures.

Recently, one of us published a short paper²¹ reporting on multilevel Monte Carlo simulations of the vortex matter in the highly anisotropic high-temperature superconductor BSCCO. We introduced low concentration of columnar defects satisfying $B_\phi \leq B$. Both the electromagnetic and Josephson interactions among pancake vortices were included. The nanocrystalline, nanoliquid, and homogeneous liquid phases were identified in agreement with experiments. We observed the two-step melting process and also noted an enhancement of the structure factor just prior to the melting transition. We also proposed a simple theoretical model to explain some of the findings. In this paper, we would like to give more details of the simulation results, but we use a different method than in the previous work, i.e., we use molecular dynamics instead of multilevel Monte Carlo. This enables us to carry out dynamical measurements that clearly identify the second melting transition (delocalization). We also report in this paper simulations of tilted columnar defects. A short summary of our findings for tilted defects has recently been submitted.²⁷

Molecular dynamics (MD) is a powerful tool for simulations of physical systems and it often serves as an alternative to Monte Carlo (MC) simulations. Its advantage is that it can be used to investigate the real dynamics of the system as opposed to MC simulations that are used for obtaining equilibrium properties. However, MD simulations could be plagued by the absence of ergodicity when applied to systems represented by path integrals,²⁸ and there is also the problem of implementing permutations for the case of identical particles like Bosons. The problem of ergodicity is really not much of an issue for Langevin simulations since the thermal noise helps the system explore the configuration space, and it can be shown by using the corresponding Fokker-Planck equation that equilibrium is reached in the long time limit. For flux lines, we have found a way to implement “permutations” in the MD simulations by flux cutting and recombining, and this was explained in a recent publication²⁹ which reported on MD simulations of the melting transition in pure BSCCO without columnar or point

defects. We were also able to implement periodic boundary conditions in all directions (including the z direction), and to include the in and out of plane electromagnetic interactions as well as the Josephson interaction using the approximation we have recently obtained.³⁰ Results for the first-order melting transitions in BSCCO for fields of 100–200 G were found to be in excellent agreement with the results of our previous multilevel Monte Carlo simulations,^{21,31} including the proliferation of nonsimple loops corresponding to flux entanglement above the melting transition. In this paper, we extend the MD simulations to systems with columnar defects, both for the case that the columns are parallel to the c axis and for the case when the columns are tilted at an angle θ with respect to the c axis. The external field is taken to be aligned along the c axis. We would like to check if the location of the melting transition in the B - T plane is sensitive to the tilting angle of the columnar defects. Recently, experiments were carried out to investigate this problem.²⁷ The conclusions were that while static thermodynamical signatures like the location of the melting and delocalization lines do not depend (within the experimental errors) on the angle between the applied field and the columnar defects, nonequilibrium properties like the position of the irreversibility line do depend on the angle.

II. SIMULATION METHOD

A. Method

In this paper, we use the London-Langevin molecular dynamics simulation method. The details of the simulation method for a system without columnar defects is given in our previous paper.²⁹ Here, we summarize the main ingredients of the method. The equation of motion for the m th pancake vortex is

$$d\eta \frac{d\mathbf{R}_m}{dt} = -\nabla_m V(\{\mathbf{r}_n\}) + \mathbf{f}_L + \boldsymbol{\zeta}_m(t). \quad (2.1)$$

The pancake label m stands actually for two indices (i, p) , where p is the plane label and i is the pancake label in that plane. The position \mathbf{R}_m is a two component vector in the plane. We use the overdamped model for vortex motion, in which the velocity of the vortex is proportional to the applied force and η is the viscous drag coefficient per unit length given by the Bardeen-Stephen expression.³² In Eq. (2.1), d is the interlayer spacing between CuO_2 planes, which is taken to be equal to the width of the pancake vortex. V is the potential energy depending on the position of all pancakes and includes both the magnetic energy and Josephson energy, and the interaction between a pancake and the columnar defects. The force is minus the gradient of the potential energy with respect to the position of the m th pancake. \mathbf{f}_L is a driving force (if present), for example, the Lorentz force induced by a current. $\boldsymbol{\zeta}_m$ is a white thermal noise term which satisfies

$$\langle \zeta_m^\alpha(t) \zeta_n^\beta(t') \rangle = 2kT\eta d \delta_{\alpha\beta} \delta_{mn} \delta(t - t'). \quad (2.2)$$

In Eq. (2.2), α and β refer to the x and y components of the vector $\boldsymbol{\zeta}$, and m and n are pancake labels. k is Boltzmann’s constant. In the simulations we use a discrete form of

the Dirac delta function. We measure distances in units of $a_0 = \sqrt{2\phi_0/B\sqrt{3}}$, where B is the magnetic field. We measure energy in units of $\epsilon_0 d$, where $\epsilon_0(T) = (\phi_0/4\pi\lambda)^2$ is the basic energy scale per unit length and λ is the penetration depth. We measure time in units of $\eta a_0^2/\epsilon_0$. For example, for $T = 60$ K and $B = 100$ G, $a_0 \approx 4887$ Å and $\epsilon_0 d \approx 4.685 \times 10^{-14}$ erg ≈ 339.5 Kk. Reference 33 quotes a value of η for a single crystal BSCCO of around 1×10^{-7} g/(cm s). Based on this value, the time unit is about 0.765 ns. These values change when the temperature and field are varied. The simulation cell was chosen to have a rectangular cross section of size $L_1 \times L_2 = a_0 \sqrt{N_{fl}} \times a_0 \sqrt{3N_{fl}}/2$, where N_{fl} is the number of flux lines (number of pancake vortices in each plane). We usually worked with 36 flux lines, but to check for finite size effect, we also used 64 FLs in some simulations. The aspect ratio of the cell was chosen to accommodate a triangular lattice without distortion, such that each triangle is equilateral. In the z direction, we take N_p layers of width d each, where, in practice, we have chosen N_p to be 36 or 200, as will be indicated below. Thus, the number of pancakes used is from 1296 up to 7200. Note that our system is effectively bigger since every pancake interacts not only with all other pancakes in the simulation cell, but with infinitely many images of these pancakes in neighboring cells in all directions.

B. Interactions

The electromagnetic (EM) interaction occurs between any pair of pancakes. To produce more realistic results for the small system simulated, we have implemented periodic boundary conditions (PBCs) in all directions including the z direction. Periodic boundary conditions mean that every pancake interacts not only with the actual pancakes in the simulation cell, but also with all their images in other cells which are part of an infinite periodic array. Each image of a pancake is located at the same position in the corresponding cell as the original pancake in the simulation cell. The details are explained in Ref. 29. The final expression we used for the pair energy of two pancakes with fully implemented PBC is

$$\frac{U_{\text{mag}}(\mathbf{R}, \Delta p \neq 0)}{\epsilon_0 d} \approx \frac{d}{\lambda} f_m(\Delta p) \left[G_0\left(\frac{\mathbf{R}}{\lambda}, \frac{L_1}{\lambda}\right) - G_{0C}\left(\frac{x}{L_1}, \frac{y}{L_2}\right) \right] \quad (2.3)$$

for pancakes in different planes separated by a vertical distance $d\Delta p$ and a lateral separation $\mathbf{R} = (x, y)$, and similarly,

$$\frac{U_{\text{mag}}(\mathbf{R}, 0)}{\epsilon_0 d} \approx 2G_{0C}\left(\frac{x}{L_1}, \frac{y}{L_2}\right) + \frac{d}{\lambda} f_m(0) \left[G_0\left(\frac{\mathbf{R}}{\lambda}, \frac{L_1}{\lambda}\right) - G_{0C}\left(\frac{x}{L_1}, \frac{y}{L_2}\right) \right] \quad (2.4)$$

for pancakes in the same plane. The functions $G_0(\mathbf{R}/\lambda, L_1/\lambda)$ and $G_{0C}(x/L_1, y/L_2)$ represent the periodic screened and bare Green's functions for the Coulomb interactions in two dimensions and are given in the Appendix of Ref. 29. The factor f_m comes from the summation of the EM interaction between a pancake and another pancake in the same cell and

all its images along the z direction. It is given by

$$f_m(\Delta p) = \sum_{l=-\infty}^{\infty} \exp(-|\Delta p + N_p l| \mu) = \frac{\exp(-|\Delta p| \mu) + \exp[(|\Delta p| - N_p) \mu]}{1 - \exp(-N_p \mu)}, \quad (2.5)$$

where we put $\mu = d/\lambda$. The dependence of f_m on Δp is rather weak. The approximations are valid provided $dN_p < \lambda$.

We have also implemented the Josephson interaction among adjacent pancakes belonging to the same FL.²⁹ Note that some authors neglect the Josephson interaction altogether for BSCCO, and this allows them to investigate considerably larger systems.¹⁹ However, we have shown^{29,31} that the inclusion of the Josephson interaction is important to obtain a realistic melting temperature that agrees with experiments and to obtain the correct scaling of the phase boundary in the B - T plane.

The approximate formula we use is based on our recent paper that derives a numerical solution to the nonlinear sine Gordon equation in two dimensions.³⁰ The formula interpolates between an $\epsilon_0 d(R/\Lambda)^2 \ln(\Lambda/R)$ dependence for small R to $\epsilon_0 dR/\Lambda$ dependence for large R , where R is the lateral separation of the pancakes, $\Lambda = \gamma d$, γ is the anisotropy, and d is the interplane separation. This interpolation is a modification of a similar interpolation formula previously used by Ryu *et al.*³⁷ The Josephson interaction diminishes with increasing anisotropy, and we choose the anisotropy parameter to be 375 to obtain reasonable agreement with recent experiment on pristine melting. In this work, we neglect Josephson interaction between pancakes belonging to different stacks because, on the average, those pancakes are farther away. In addition, we view the stack as the collection of pancakes carrying the unit quantum of flux from one side of the sample to the other. Since the Josephson interaction is proportional to the gauge invariant phase difference $\Delta\varphi + (2\pi/\phi_0) \int ds \cdot \mathbf{A}$, the second term involving the vector potential will be larger for pancakes belonging to the same stack than for pancakes belonging to different stacks. This argument works in the solid phase but not deep into the liquid phase, where, eventually, stacks may lose their meaning, especially if the density of pancakes is large so that the average distance is much smaller than λ (high temperatures and high fields).

Since the Josephson interaction is between nearest neighbor pancakes in adjacent planes, it is quite straightforward to implement PBC. A pancake at the top plane (N_p) interacts with the closest pancake in the bottom plane 1 as well as with a pancake in plane $N_p - 1$. When calculating the lateral distance between pancakes, we always measure the “shortest distance” defined as follows: If the actual $|\Delta x|$ separation is larger than $L_1/2$, we subtract or add L_1 depending on the sign of Δx , and similarly for Δy , with L_2 replacing L_1 . This way, the correct distance is obtained even when the adjacent pancake in the plane above has exited the simulation cell and emerged close to the other side of the simulation cell.

In the case of $R \gg r_g$, string-string interactions that involve three- and four-body interactions become important.³⁴ How-

ever, near the melting transition for the range of magnetic fields investigated in this paper, $R \approx 0.25a_0 \approx 1000 \text{ \AA}$, whereas $r_g \approx 5625 \text{ \AA}$. Thus, large transverse fluctuations for which the string-string interactions become important are statistically rare and can be neglected. Even in the case of tilted CDs we verified that the kinks present (see later discussion) are not fully developed Josephson strings. Thus, in this work, we do not include string-string interactions.

The modeling of the interaction between pancakes and CDs was discussed by Goldschmidt and Cuansing.²¹ There are two major sources of pinning: core pinning and EM pinning. Core pinning² arises when the vortex core overlaps with a normal state inclusion similar to the one inside a CD. Since condensation energy is lost in the vortex core, part or all of this energy is restored when a vortex resides inside a CD. EM pinning arises^{35,36} when the supercurrent pattern around the vortex is disturbed by the nonconducting defect. These two mechanisms combine together to yield the expression for the potential energy at a distance R away from the CD as felt by an individual pancake:^{2,36}

$$V(R) \approx \begin{cases} \epsilon_0 d \ln \left[1 - \left(\frac{r_r}{R + \xi/\sqrt{2}} \right)^2 \right], & R > r_r \\ \epsilon_0 d \ln \left[1 - \left(\frac{r_r}{r_r + \xi/\sqrt{2}} \right)^2 \right], & R < r_r, \end{cases} \quad (2.6)$$

where r_r is the radius of the CD. The long range tail contribution $\approx -\epsilon_0 d r_r^2 / R^2$ is due mainly to the EM pinning, and the short range flat region of depth $\approx \epsilon_0 d$ is due to the combined effects of EM and core pinning. This formula is valid provided $r_r > \sqrt{2}\xi$. If $r_r < \sqrt{2}\xi$, a slightly different expression should be used, but we have determined (see below) that in order to get good agreement with experiments, we need to use $r_r > \sqrt{2}\xi$. Note that in this expression, ϵ_0 is temperature dependent and is proportional to $1 - T/T_c$. For example, the pinning strength reduces to realistic values of 113 K at $T = 80$ K and of 79 K at $T = 83$ K assuming $T_c = 90$ K.

After experimenting with CDs of different radii ($10 \text{ nm} \leq r_r \leq 30 \text{ nm}$), we concluded that in order to obtain good agreement with experimental results, we needed to choose $r_r \approx 30 \text{ nm}$, in which case the formula given by Eq. (2.6) is the correct one. Different heavy ions with different energies give rise to tracks of various sizes, normally reported to be in the range of 4–20 nm in diameter. It may be that the actual damage caused by a track exceeds its apparent size, thus leading to a higher effective radius. For tilted CDs, it may be appropriate to take a potential with an elliptical cross section rather than a circular one. Since our simulations for tilted CDs are mainly for angles of 45° which are not that large and since the radius of our CDs is already larger than the actual experimental radius, we did not use elliptical cross sections in the present simulations.

C. Details of the simulations

The simulation cell is divided into an 800×692 mesh of small cells of area $\tilde{h} \times \tilde{h}$ each, where $\tilde{h} = \sqrt{N_{fl}}/800$ (in units of a_0). We tabulated the functions G_0 and G_{0C} using a less refined cell structure, creating two large 200×174 matrices.

During the simulations, we used the tables as a lookup to calculate the pair interaction and used interpolation to find the applicable values. For each table, we also calculated the negative of the gradient and saved the two components of the gradient in their own tables. We also tabulated the Josephson interaction and its gradient and the columnar defect potential and its gradient, but for these quantities, we used 800×692 matrices. When simulating, we allowed pancakes to move to arbitrary real locations, but in order to calculate the forces, we divided the actual position by \tilde{h} and rounded to the nearest integer to use for the lookup tables.

In each simulation step, we moved all the pancakes at the same time, using the instantaneous forces. This is done using a time step $\Delta\tilde{t}$. In these simulations, we used the second-order Runge-Kutta method to advance the solution of the differential equations, which requires an additional virtual move for any real move. It is very important to choose the time step correctly, especially when CDs are present. We used a variable size time step that limits how much a pancake can move in each step. The maximum distance allowed was $0.06a_0$. Thus, if the maximum force on the pancakes is very large, a small time step is used.

In the simulation, we applied a procedure to implement flux cutting and recombination. We assumed that within the coupled-planes model, vortices may switch connections to lower their elastic energy (in this case, Josephson energy) when they cross each other.³⁷ In the simulation, we constructed two matrices of size $N_{fl} \times N_p$, which we call the “up” matrix and the “down” matrix. For a given pancake i in plane p , the up matrix points to the pancake in the plane $p+1$ (or 1 if $p=N_p$) that is connected to the given pancake (i, p) via a Josephson interaction. Generally, this is the pancake closest to the given pancake in the next plane. The down matrix similarly points to the closest pancake below (or in plane N_p for $p=1$). When we start from an initial configuration in which the FLs are straight stacks of pancakes, the matrices simply point to the pancake just above or below a given pancake. When constructing the force matrix after each time step, we check if, indeed, the up matrix points to the closest pancake above. If there is a closer pancake than the one given by the pointer, then we find out its parent in the plane p by using the down matrix, and we check if switching the two connections will decrease the sum of the squares of the two distances. If it does, we cut and switch connections and update the up and down matrices. We term this process an *exchange*. The reason we use the square of the distances is that in most instances the Josephson interaction is proportional to the square of the transverse distance. This procedure mimics the actual dynamics in which we expect the magnetic flux to choose a path that minimizes the Josephson energy. We implement the flux cutting procedure after every update move of the system, but not during the virtual half-step in the Runge-Kutta procedure.

Our simulations show that just below the melting transition, even though some exchanges occur, they soon reverse or undo themselves, and thus, they do not lead to what we refer to as an entangled state where composite loops or permutations are abundant. On the other hand, when exchanges proliferate through the system, a phenomenon that occurs in

our simulations just above the melting transition, the exchanges do not undo each other, and the system of FLs changes from being composed of simple loops, each made up of a single FL ending on itself, to a system composed mainly of composite loops that wind up several times around the simulation cell in the z direction before returning to the original point. The reason that the exchanges proliferate above the melting transition is that the transverse fluctuations become strong enough to overcome the potential barriers due to the repulsion among pancakes residing in the same plane, and thus, the crossing of FLs occur.

D. Measured quantities

We measured the following physical quantities. For details, the reader is referred to our earlier work.^{18,31} The translational structure factor was also measured, but we do not report on it in the present paper.

1. Energy

We calculated the average energy per pancake. The total energy is the sum of the contributions from the EM energy of all pairs of pancakes, the Josephson energy of nearest neighbor pancakes in adjacent planes, and the binding energy of pancakes trapped by columnar defects. For the first part, the EM energy of a perfect Abrikosov lattice at the same temperature and magnetic field was subtracted from the total EM energy.³⁸

2. Mean square deviations

For each individual flux line, we define the position of the lateral center of mass as $\mathbf{R}_{c.m.} = \sum \mathbf{R}_{(i,p)} / N_p$, where the sum goes over all the pancakes belonging to it. We then define the mean square deviations as

$$R_f^2 = \left\langle \sum (\mathbf{R}_{(i,p)} - \mathbf{R}_{c.m.})^2 \right\rangle, \quad (2.7)$$

where the sum is over all pancakes belonging to an individual flux line, and the average is over all flux lines of the system and then taking a time average. The melting transition is expected to occur when this quantity satisfies

$$R_f/a_0 \geq c_L, \quad (2.8)$$

where c_L is the Lindemann coefficient.

3. Line entanglement

As we allow for flux cutting and recombination, we can define the number N_e/N_{fl} as that fraction of the total number of FLs which belong to loops that are bigger than the size of a “simple” loop. A simple loop is defined as a set of N_p beads connected end to end (due to the periodic boundary conditions in the z direction). Loops of size $2N_p, 3N_p, \dots$, start proliferating at and above the melting temperature.

4. Drift velocity under an applied force

For the dynamical measurements, a uniform driving force of proper magnitude was applied along the positive x direction. The average drift velocity of each pancake was mea-

sured. Both the distribution and the average value of these velocities are studied. They provide evidence on the delocalization transition and the melting transition.

5. Parameters

Parameters for BSCCO were taken as follows: $\lambda_0 = 1700$ Å, $d = 15$ Å, $\xi_0 = 30$ Å, and $T_c = 90$ K. The temperature dependence of λ in this work was taken to follow the Ginzburg-Landau convention $\lambda^2(T) = \lambda_0^2 / (1 - T/T_c)$, and similarly for ξ . See discussion in Ref. 31 on the agreement of this choice with experiments. For the anisotropy γ , we have used the value of 375. For columnar defects, we have used a radius of 30 nm.

III. VERTICAL COLUMNAR DEFECTS

In this section, we concentrate on the simulations of systems with vertical CDs. Both static measurements and dynamical measurements have been done. For the static measurements, we start from a hexagonal lattice of straight and vertical FLs. The CDs attract those FLs which are near them and rapidly become occupied. For temperatures close to and above the melting transition, the FLs also become entangled. It takes a relatively long time for the entangling process to reach equilibrium, especially near the transition. We took 50 units of model time (time is measured in units of $\eta a_0^2 \epsilon_0$) for equilibration and another 50 units of model time on measurements. Simulations have been done on systems with 36 FLs and 36 layers. Columnar defect density B_ϕ was set to be 50 G. Magnetic fields from 50 to 200 G were investigated. For each field value, ten different CD configurations were simulated and the measurement results were averaged.

According to the periodic boundary condition along the z direction, the top of each FL is connected via the Josephson interaction with the nearest pancake in the bottom plane. Below the melting transition, the pancake usually belongs to the same FL as the top pancake. We say that the FLs form simple loops. As temperature increases, the thermal motion of the pancakes starts to make some pairs of FLs get close enough that flux cutting and reconnection happen, and some FLs become part of a nonsimple loop. Figure 1(a) shows the fraction of FLs belonging to nonsimple loops. Below the melting transition, none of the FLs entangle with others and the curves lie exactly at zero; above the delocalization transition, a nearly uniform liquid is formed and the curves approach 1. The criteria for melting can be taken to be that the fraction of nonsimple loops reaches $\approx 0.1-0.2$. It shows that the melting temperature decreases as the magnetic field increases. Figure 1(b) shows the average mean square deviation of the pancakes on each FL relative to their “center of mass.”²⁹ The results are in units of a_0^2 for $B = 100$ G. The melting transition is characterized by the sharp change of slope. For example, for $B = 50$ G, the change happens around a reduced temperature $T/(1 - T/T_c)$ of 600 K, which corresponds to $T = 78$ K, with mean square deviation $\approx 0.1-0.2$.

Another quantity of interest is the number of trapped pancakes. Usually, each CD is occupied by a single FL. The trapped FLs form a cage for the interstitial FLs. Below the melting, the interstitial FLs form crystallites in the pores. At

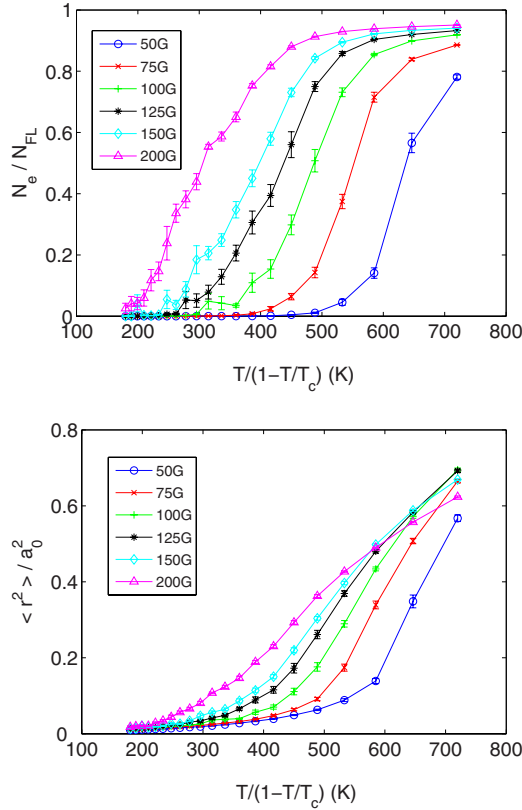


FIG. 1. (Color online) Static simulations for systems of 36 layers with $B_\phi = 50$ G and different values of B . The curves are averaged over ten CD realizations. (a) Fraction of FLs belonging to nonsimple loops. (b) Mean square deviations of FLs.

temperatures slightly above the melting transition, the crystallites melt locally and form a nanoliquid in the pores. Higher temperature enables the trapped FLs to escape out of the CDs and the cage also melts, so a homogeneous liquid is formed. To compare results of different magnetic fields, Fig. 2(a) plots the fraction of occupied CDs, which is given by the fraction of trapped pancakes multiplied by FL to CD ratio. As a common character for all the field values, the fractional values decrease as temperature is increased. The curve for $B = 50$ G is significantly lower than that of higher field values at low temperatures. Even though the FL to CD ratio is 1, the repulsion between the FLs tries to make them evenly spaced, and some FLs have to be interstitial and some defects become unoccupied. Figure 2(b) shows the normalized binding energy, which is the binding energy per plane per CD. As a consequence of Fig. 2(a), the values increase as the temperature increases because the fraction of occupied CDs decreases. As a comparison with our previous work,²¹ Fig. 2(c) is the average binding energy per pancake.

In order to verify that our system is large enough and finite size effects will not significantly change the results, we carried out simulations with 64 FLs in 36 planes. A comparison between the results of 36 and 64 FLs is depicted in Fig. 3. We see that the results are very similar: the transition for 64 lines is slightly sharper, but this is not a significant effect.

Next, we discuss the dynamical measurements which were performed in order to locate the delocalization transi-

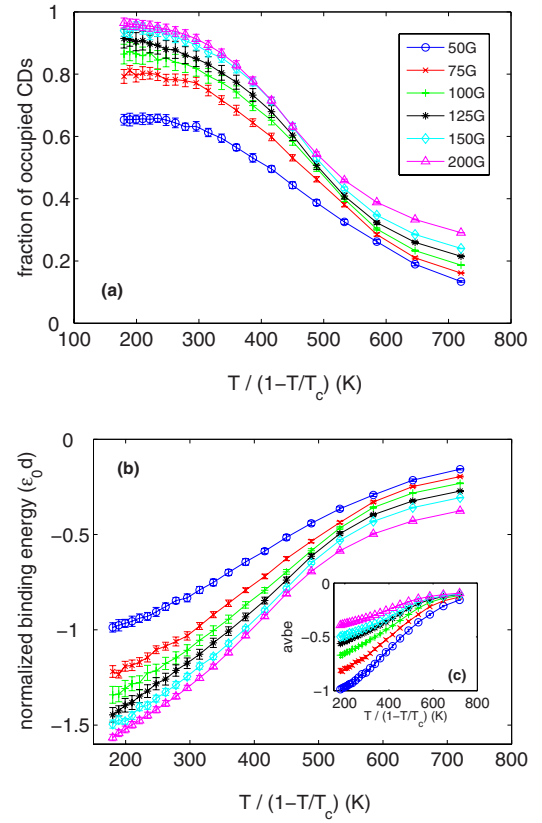


FIG. 2. (Color online) Static simulations for systems of 36 layers with $B_\phi = 50$ G and different values of B . The curves are averaged over ten CD realizations. (a) Fraction of occupied CDs. (b) Normalized binding energy. (c) Average binding energy per pancake. (b) and (c) used the colors as in (a) to represent different magnetic fields.

tion and the irreversibility line. The system is also started from a hexagonal lattice of straight and vertical FLs. After 20–50 units of model time for equilibration without driving force, a uniform in-plane driving force f_L is applied on all the pancakes along the x direction. We used $f_L = 0.025$ and 0.1 , which are small compared with the binding force on the trapped pancakes. Five to thirty units of model time were used on equilibration with driving force, and 20–50 units of model time were used on measurements.

Under a driving force, the interstitial pancakes are much easier to drift relative to the trapped ones. For driving force $f_L \lesssim 0.1$ and below the delocalization transition, most of the trapped pancakes remain trapped during the time span of our simulation. The average velocity of each pancake during the finite time of measurement has been recorded. Figure 4 shows its distribution for temperatures near the delocalization transition. The distribution is normalized so that the area of the region under the curve is 1. Below the transition temperature, the distribution is characterized by a sharp peak at zero, and a wider and lower peak centered above zero. The sharp peak corresponds to the trapped pancakes, and the wide peak corresponds to the interstitial ones. The driving force we used was small enough that the trapped pancakes would not be pulled out of the columnar defects below the delocalization transition, but large enough that the interstitial

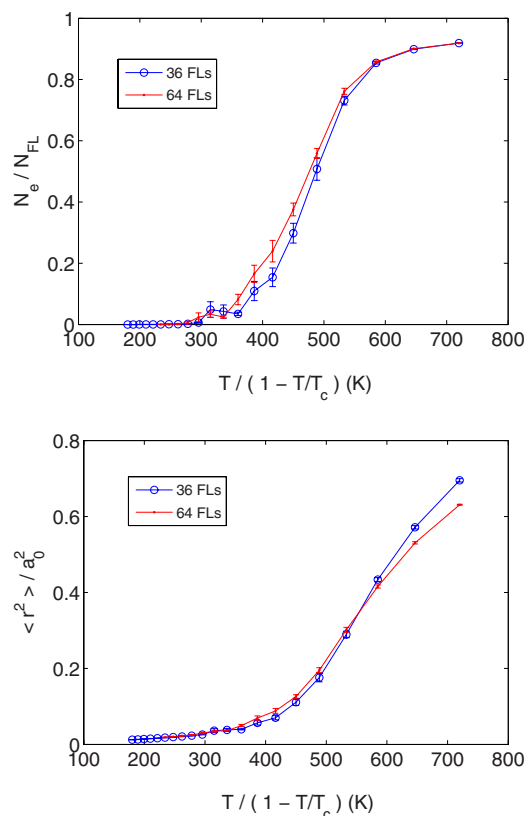


FIG. 3. (Color online) Static simulations for systems with 36 FLs (blue curves with circles) and 64 FLs (red curves). The curves are averaged over ten CD realizations. $B=100$ G and $B_\phi=50$ G. (a) Fraction of nonsimple loop FLs. (b) Mean square deviations of FLs.

pancakes could move through the skeleton formed by trapped FLs. As temperature increases, the height of the sharp peak decreases and the wide peak becomes wider. The sharp peak disappears above the delocalization temperature and the center of the remaining Gaussian shaped wide peak

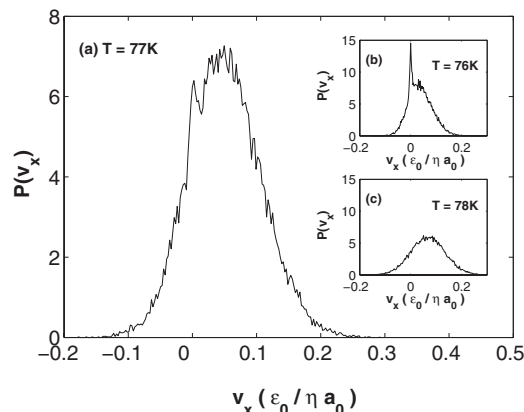


FIG. 4. Normalized distribution of average velocity along the x direction. $B=100$ G, $B_\phi=50$ G, and simulation of system with 36 FLs and 200 layers. The driving force f_L was taken to be 0.1 and four different CD configurations were done. (a)–(c) are the distributions at temperatures in the vicinity of the delocalization transition.

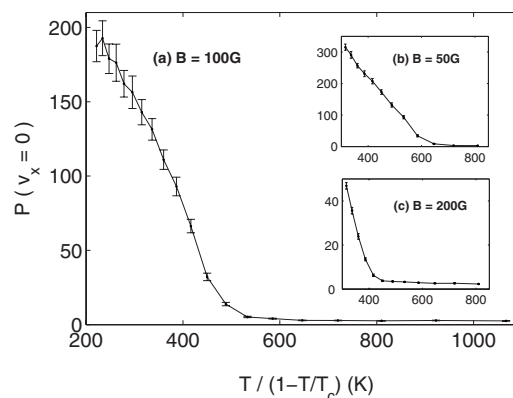


FIG. 5. Probability density of zero average velocity at various temperatures. Results for three different fields are shown here. Simulations on systems with 36 FLs and 36 layers. $B_\phi=50$ G and driving force $f_L=0.1$. Averaged over ten different CD configurations.

approaches 0.1, which is the value of the driving force.

One should notice that the width and height of the distribution in Fig. 4 depend on the length of the measurement. The longer the measurement is, the narrower and taller the wide peak is. For random walk, the average distance the walkers travel is proportional to the square root of time, thus the average velocity of the walkers decreases as the time of averaging becomes longer. The movement of the interstitial pancakes are different from a simple random walk. They are confined by other FLs, especially by the trapped ones. They are also confined by pancakes in adjacent layers through Josephson interaction. However, our simulations do show that the width of the wide peak times the square root of the time span of the measurement is roughly constant near and above the delocalization transition.

In Fig. 5, the probability density of zero average velocity, i.e., the value of the average velocity distribution at zero, is plotted. Results for magnetic fields of 50, 100, and 200 G are shown. The delocalization transition is characterized by the abrupt change of the slope of the plotted curves, which happens around reduced temperatures of 600, 500, and 400 K, respectively, corresponding to 78, 76, and 73 K. The delocalization transition temperature decreases as the magnetic field increases.

It is possible to locate the irreversibility line from the time averaged drift velocities by taking an average over all pancakes. The average velocity of the pancakes is depicted in Fig. 6. For temperatures below the irreversibility line, which is the threshold of mobility as a function of temperature, the curves are flat and the drift velocity is small. Then at a temperature about equal to the melting temperature, their slopes increase sharply. The sharp rise in mobility is most clear for the $B=50$ G case, for which the melting transition and the delocalization transition happen at the same temperature. At low temperatures, the FLs are pinned collectively by the CDs. They are nearly immobile under a small driving force. When the temperature is raised high enough that the interstitial pancakes can move easily in the pores, a small driving force will make the FLs drift, signaling the onset of depin-

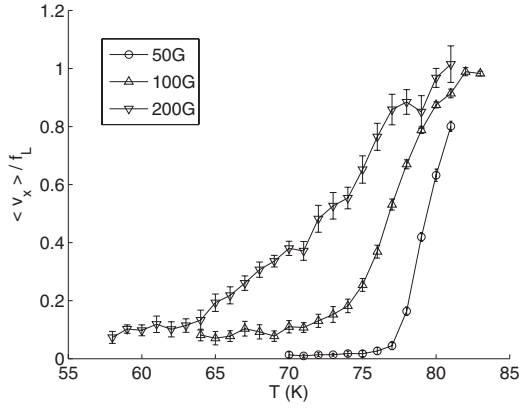


FIG. 6. Average drift velocity over driving force. Results with magnetic fields of 50, 100, and 200 G are shown. The same data as in Fig. 5 for $B=50$ G and $B=100$ G, where $f_L=0.1$ was used. For $B=200$ G, $f_L=0.025$ was used.

ning. Above the delocalization temperature, the trapped pancakes also start to drift under the small driving force, making the ratio of average drift velocity over driving force approach 1.

The results above are summarized into a phase diagram (Fig. 7). It is divided into three regions by the melting line B_m^{cd} and the delocalization line B_{dl} . Between these two lines, the vortex system is in a nanoliquid phase, in which the interstitial FLs are entangled and melted, but are separated from the trapped FLs. To the left of the dashed line associated with the melting line, the system is in the nanocrystal phase, in which all the FLs are separated from each other; the interstitial ones form triangular lattices in the pores surrounded by the trapped ones. The error bars indicate the width of the transition region due to the finite size of our system. The melting line B_m^0 of a pristine system is also plotted for comparison.

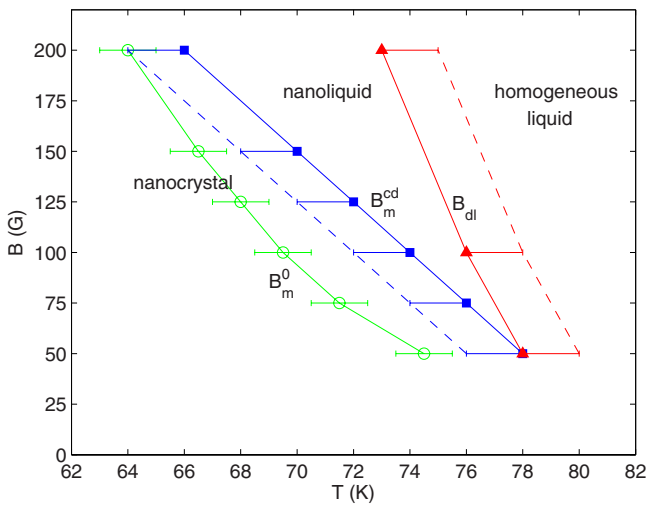


FIG. 7. (Color online) Phase diagram in the T - B plane. The melting transition B_m^0 of pristine system, the melting transition B_m^{cd} of system with columnar defects ($B_\phi=50$ G), and the delocalization transition B_{dl} of system with columnar defects ($B_\phi=50$ G) are shown.

ted for comparison. To the right of the dashed line associated with the delocalization line, the system is in a homogeneous liquid phase, where the effect of the CDs becomes less important and all the FLs become entangled.

IV. TILTED COLUMNAR DEFECTS

It is interesting to study the effect of the tilting of CDs on the properties of the vortex system. Hwa *et al.*,³⁹ Nelson and Vinokur,^{22,40} and, more recently, Refael *et al.*⁴¹ studied the effect of a tilted magnetic field on the properties of the Bose glass system. In their investigation, the CDs are along the c axis and the magnetic field has a component H_\perp along the a - b planes, thus forming an angle θ between the direction of the applied field and the CDs. When the angle θ is small, the vortices which are localized on the CDs are completely trapped along the CDs and the Bose glass phase is preserved. At larger $\theta > \theta_c$ ($H_\perp > H_c^c$), the vortices form a staircase structure, hopping from one CD to the next. For different vortices, those kinks tend to align in “chains.” For an even larger angle $\theta > \theta_a$, the vortices follow the field direction and are essentially unaffected by the correlated nature of the CDs. This picture appears to describe correctly the situation in YBCO in the Bose glass regime ($B < B_\phi$) and is supported by various experiments, both for thermodynamical⁴² and dynamical properties.^{43,44}

For BSCCO which is much more anisotropic, the situation appears more complicated and less clear.^{45,46} Furthermore, in this case, there are interesting results on the nanosolid phase which exists for $B > B_\phi$ and is different from the Bose glass phase. There are no theoretical investigations on how the nanosolid phase and its two stage melting transition might be affected by a tilting angle between the direction of the CDs and the magnetic field. To try to answer this question, we recently carried out experiments and numerical simulations to try to understand the properties of such a system.²⁷ Here, we give more details on the method and the results of the simulations.

In this work, we limited our investigation to the case of a vertical external magnetic field (parallel to the c axis) and considered only the case of tilted CDs at various angles. Simulations with 36 layers are not enough any more, since the shift of the top of the CDs relative to their bottom would be too small. We used 200 layers, which is still manageable by the current computing power. Most of the simulations were done on systems with 36 FLs and 18 CDs. The magnetic field was set to be 100 G. For comparison, both systems with vertical CDs and systems with tilted CDs were simulated. The comparison between the two systems was done for the same value of $B_\phi^{\text{eff}} = B_\phi \cos \theta$ in order to match the experimental situation, in which the ratio of vortices to CDs remains fixed as θ changes.²⁷ Both static and dynamical measurements were carried out, and the results are averaged over four different random CD configurations.

Figure 8 shows the results of static measurements. Figure 8(a) shows the fraction of occupied CDs, i.e., the number of trapped pancakes over the number of trapping sites. Over the temperature range of our simulations, the vertical case and the tilted case give the same results within the error bars. At

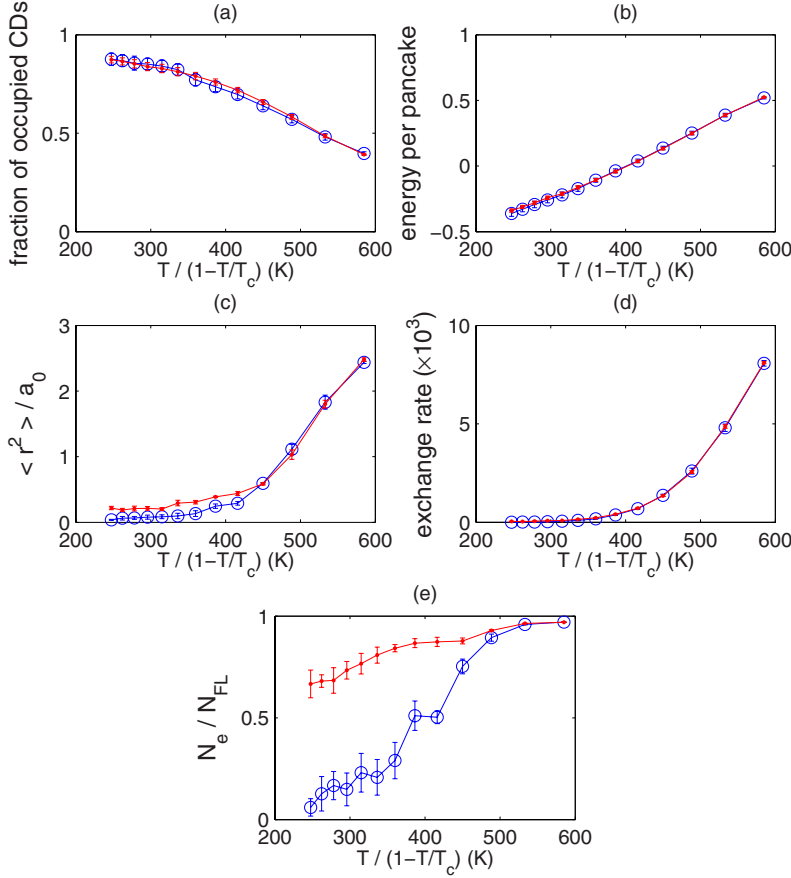


FIG. 8. (Color online) Static measurements on systems with vertical CDs (blue curves with circles) and tilted CDs (red curves; CDs are tilted by 45° away from the c axis). (a) Fraction of occupied CDs. (b) Total energy per pancake. (c) Mean square deviation of FLs. (d) Exchange rate. (e) Fraction of FLs belonging to nonsimple loops.

reduced temperatures below 350 K, the ratio is close to 1, so the CDs are almost fully occupied. In Fig. 8(b), the total energy per pancake are almost the same in the two cases. In Fig. 8(c), the mean square deviation of the FLs in the tilted case is a little higher than that of the vertical case at low temperatures. Since our measurements are relative to the center of mass of each FL, and as will be shown later, the FLs are tilted by the tilted CDs, the deviations are raised to higher values. The sudden change in the curves' slopes reflects the position of the melting transition of the interstitial FLs. Figure 8(c) might suggest a 1° increase in the melting temperature for tilted CDs, but this is within the simulation error. Figure 8(d) shows the number of “exchanges” per unit time, i.e., the rate of cutting and recombining of FLs. This number is under 1000 below the melting transition, and increases rapidly above the melting. We see that it is the same for both straight and tilted CDs. Figure 8(e) shows the amount of entanglement, i.e., the fraction of nonsimple loops. The flat area of the curves is an indication of the melting transition. First, we note that for straight CDs, the fraction of nonsimple loops at the transition for 200 layers is higher than the corresponding value for 36 layers, which is about 0.2. This is because for longer FLs, there are more chances to cross and also to form occasional kinks involving the CDs. This figure is the only one that shows a significant difference between the straight and tilted CDs in terms of the absolute value of their entanglement. This is likely due to the fact that FLs trapped on CDs are tilted and so are those FLs in the vicinity of a CD. Thus, the top and bottom of those

FLs are not adjacent, and they may connect to other FLs to form loops. This interpretation is favored by the fact that the number of exchanges for the tilted CD case is not larger than for the case of straight CDs, but the amount of their entanglement is larger nevertheless. Thus, this criterion (of entanglement) using the boundary conditions may not be a good indication of the melting transition in the case of tilted CDs as it is for the case of a pure system or a system with straight CDs. The flat plateau region of the curve should give a rough indication where the melting takes place. Thus, for tilted CDs, we base our criterion for the melting on the transverse fluctuations of the FLs and on the number of exchanges per unit time rather than on the amount of entanglement.

We now account for the energies involved: The electromagnetic energy cost per layer associated with the tilting of an infinitely long stack of pancakes is given by¹⁰ $\epsilon_0 d \ln[(1 + \cos \theta)/2 \cos \theta]$. This cost is exceeded, for angles less than about 75° , by the energy gain from the pinning of columnar defects, which is of the order of $\epsilon_0 d$ per layer. In addition, one should also include the energy $-\mathbf{B} \cdot \mathbf{H}/4\pi$, which favors the alignment of the average vortex orientation with H , which in our case points in the z direction. The variable H is not represented directly in our model. However, in the simulations, an extra restoring force that tries to align the pancakes in the z direction arises from the way we implement the periodic boundary conditions: When a stack is tilted, the stacks of images along the z direction are not positioned along the tilted direction but are above (and below) the cen-

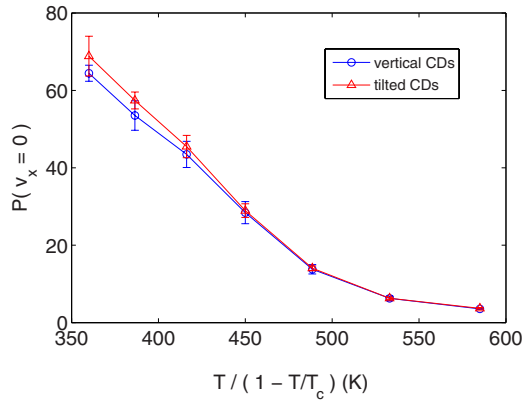


FIG. 9. (Color online) Probability density of zero average velocity. The blue curve with circles is for vertical CDs, and the red curve with triangles is for tilted CDs. Driving force $f_L=0.1$.

ter of mass of the tilted stack, and because of the electromagnetic interaction, they pull the stack in the z direction, acting similar to a $\mathbf{B} \cdot \mathbf{H}$ term. The competition between the binding energy gain and the loss of electromagnetic energy associated with a tilt favors the formation of kinks. The trapped FLs tilt to take advantage of the binding energy of the tilted CDs, and the interstitial FLs tilt because of repulsion by the trapped pancakes. However, in order to relieve the frustration of the electromagnetic interaction, kinks are formed and the FLs jump back to align with the z axis, which is the external field direction. The larger the tilting angle of the CDs, the more kinks appear along the FLs. The kinks on neighboring FLs tend to align with each other. The formation of the kinks increases the Josephson interaction part; however, in high anisotropic materials like BSCCO, this cost is negligible compared with the total energy.⁴⁷ Near the transition, the transverse fluctuations due to the tilt-kink combination are not much different from the transverse fluctuations due to temperature fluctuations. Our simulations show that the vortices form a tilted rigid matrix which is parallel to the CDs, and the CDs are almost fully decorated by pancakes. Because of the kinks, the interstitial vortices can switch cage after a certain distance along the z direction, but each section is still caged by the trapped pancakes on the CDs. Also, interstitial FLs can themselves be trapped on CDs for some portion of their length. In the vicinity of the melting transition ($T=73\text{--}77$ K), considering the error bars of the measurements, we found that systems with CDs tilted at 45° have nearly the same total energy as those with nontilted CDs. One can conclude that the enhanced caging potential created by the CDs, which raises the melting temperature,¹⁵ is not significantly affected when increasing the angle between \mathbf{B} and the CDs; thus, the thermodynamic properties, i.e., the melting transition and the delocalization, are angle independent. This has been shown in our static simulations in Fig. 8, and will be further demonstrated for the delocalization transition in the following discussion.

The effect of tilting of the CDs on the delocalization transition is also investigated. Figure 9 shows the probability density of zero average velocity for both the vertical case and the tilted case. The two curves coincide within the range of

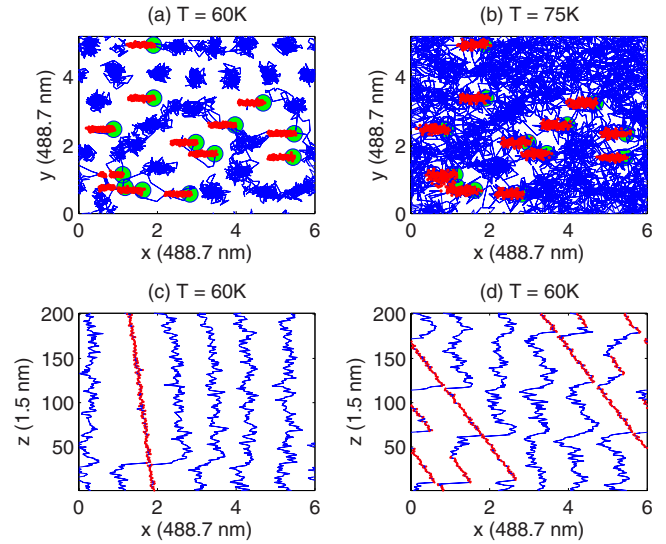


FIG. 10. (Color online) Snapshots of vortex stacks and CDs tilted at 45° [(a)–(c)] and 80° , $B_\phi^{\text{eff}}=36$ G. (d) For $B=100$ G. Pancakes belonging to the same stack are connected. Free pancakes are in blue and trapped ones in red. Only CDs at the bottom layer are shown (green). [(a) and (b)] Projection onto a - b plane (top view). (a) Nanosolid phase. (b) Nanoliquid phase. (c) Projection of (a) onto a - c plane (side view), first row is shown. (d) Side view with CDs at 80° .

the error bars, especially at temperatures near the delocalization transition. The average velocity distributions of these two cases are also compared, and one cannot see any significant difference. One can conclude that the tilting of CDs does not have a noticeable effect on the delocalization transition of the vortex system.

Snapshots are shown here on systems without a driving force. Figures 10(a) and 10(b) show the top view of a system with CDs tilted by 45° at 60 and 75 K, respectively. At 60 K, the system is in the nanosolid phase and individual FLs can be distinguished clearly. The interstitial FLs try to form hexagonal lattices. At 75 K, the system is in the nanoliquid phase. Interstitial FLs become entangled and the pancake vortices distribute nearly uniformly in the pores. However, the temperature is not high enough to make trapped pancakes delocalize yet. The nanoliquid is repelled by the trapped FLs, thus forming void spaces surrounding the CDs. Figure 10(c) is a side view of the first row of the FLs in Fig. 10(a). Usually, a CD is occupied by more than one FL and kinked structures emerge. The kinks go along the a - b plane and extend for less than ten CuO_2 layers. There are also kinks on interstitial FLs. They tend to reside at the same layers with those attached to CDs and form trains of kinks,⁴¹ which resemble the Josephson and Abrikosov crossing lattices⁴⁸ found in BSCCO, with field tilted with respect to the c axis. Another feature is that the interstitial FLs break into segments, which are tilted to some degree along the direction of the CDs. Because of the kinks, the FL segments jump back periodically, keeping the FLs vertical on average. At higher temperatures, the kinked structures and tilting of interstitial FLs still exist, but are complicated by the entanglement of the FLs. In Fig. 10(d), the CDs are tilted by a larger angle

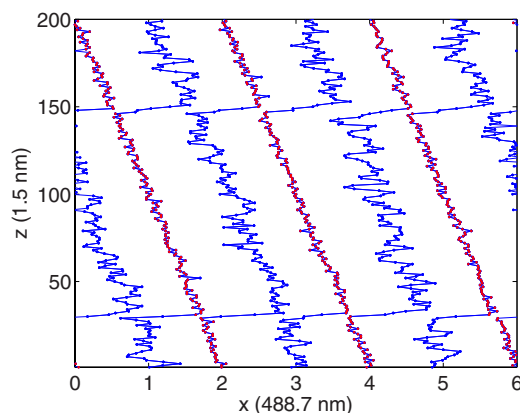


FIG. 11. (Color online) Snapshot of a 2D system with 200 planes, 6 FLs, and 3 CDs. Pancakes belonging to the same stack are connected. Trapped ones are in red and interstitial ones are in blue. CDs are evenly spaced and tilted at 73° so that they are continuous at the boundaries. $T=70$ K.

than in Fig. 10(c); as a consequence, more kinks appear and the separation between the trains of kinks becomes smaller.

Under large enough driving force and temperature in the proper range, FL kinks can move along the z direction and the pancake vortices drift along the direction of the driving force. To show this, we simulated a two-dimensional system with six FLs and three tilted CDs (Fig. 11). The pancakes were confined to move only in the x - z plane. The CDs were arranged such that they are continuous at the boundaries. We initialized the FLs to be vertical, straight, and evenly spaced. After simulating for enough time to let the system equilibrate without a driving force, two trains of kinks were formed. A driving force of magnitude $f_L=0.5$ was then applied along the positive x direction. At 70 K, the kinks moved downward altogether with a constant speed of about 13 CuO_2 planes for every ten time units.

V. CONCLUSIONS

To conclude, we have used Langevin molecular dynamics simulations to investigate the melting transition of the vortex matter in the presence of vertical CDs and in the presence of

tilted CDs. For vertical CDs, our results are in full agreement with our previous multilevel MC simulations reported in Ref. 21. Furthermore, we also measured dynamical properties of the system under an external current that applies force on the vortices and these located the melting and delocalization transitions at the same temperatures as the static measurements, giving a more precise identification of the location of the delocalization transition. For the melting transition, the dynamical measurement actually identifies the irreversibility line associated with partial depinning, and this occurs at the same temperature as the melting for the case of vertical CDs.

For the case of tilted CDs, the porous vortex matter in BSCCO is shown to preserve its thermodynamic properties even when the field is tilted away from the CDs. The positions of the melting and delocalization lines remain unchanged, while the tilting angle of the CDs varies at least up to angles of 45° . Our simulations show that increasing the angle between the field and the CDs leads to the formation of weakly pinned vortex kinks, while preserving the basic structure of a rigid matrix of pancakes residing along the CDs, with nanocrystals of interstitial vortices embedded within the pores of the matrix. We also showed that under the influence of an applied force (like a current), the kinks slide down and lead to a global motion of the pancakes in the direction of the applied force. Thus, we expect that for large tilting angle between the CDs and the magnetic field, which result in the proliferation of kinks, the irreversibility line should move to a lower temperature, closer to the location of melting in the pure system (no CDs). To measure this shift explicitly in the simulations as a function of the angle requires much more computational time than currently available, but it was verified in the recent experiments.²⁷

ACKNOWLEDGMENTS

This work was supported by the U.S. Department of Energy (DOE) under Grant No. DE-FG02-98ER45686. We also thank the DOE NERSC program and the Pittsburgh Supercomputing Center for time allocations. Y.Y.G. thanks the Weston Visiting Professors program of the Weizmann Institute of Science for support during a recent visit, and E. Zeldov for his hospitality. Y.Y.G. also thanks N. Avraham and E. Zeldov for useful discussions.

¹M. Tinkham, *Introduction to Superconductivity*, 2nd ed. (Dover, New York, 2004).

²G. Blatter, M. V. Feigel'man, V. B. Geshkenbein, A. I. Larkin, and V. M. Vinokur, *Rev. Mod. Phys.* **66**, 1125 (1994), and references therein.

³E. H. Brandt, *Rep. Prog. Phys.* **58**, 1465 (1995).

⁴H. Safar, P. L. Gammel, D. A. Huse, D. J. Bishop, J. P. Rice, and D. M. Ginsberg, *Phys. Rev. Lett.* **69**, 824 (1992).

⁵W. K. Kwok, S. Fleshler, U. Welp, V. M. Vinokur, J. Downey, G. W. Crabtree, and M. M. Miller, *Phys. Rev. Lett.* **69**, 3370 (1992).

⁶R. Cubitt, E. M. Forgan, G. Yang, S. L. Lee, D. M. Paul, H. M.

Mook, M. Yethiraj, P. H. Kes, T. W. Li, A. A. Menovsky, Z. Tarnavski, and K. Mortensen, *Nature (London)* **365**, 407 (1993).

⁷E. Zeldov, D. Majer, M. Konczykowski, V. B. Geshkenbein, V. M. Vinokur, and H. Shtrikman, *Nature (London)* **375**, 373 (1995).

⁸A. Schilling, R. A. Fisher, N. E. Phillips, U. Welp, D. Dasgupta, W. K. Kwok, and G. W. Crabtree, *Nature (London)* **382**, 791 (1996).

⁹G. W. Crabtree and D. R. Nelson, *Phys. Today* **50**, 38 (1997).

¹⁰J. R. Clem, *Phys. Rev. B* **43**, 7837 (1991).

¹¹J. R. Clem, *J. Supercond.* **17**, 613 (2004).

¹²S. N. Artemenko and A. N. Kruglov, *Phys. Lett. A* **143**, 485

- (1990).
- ¹³J. R. Clem, M. W. Coffey, and Z. Hao, *Phys. Rev. B* **44**, 2732 (1991).
 - ¹⁴A. E. Koshelev, *Phys. Rev. B* **48**, 1180 (1993).
 - ¹⁵S. S. Banerjee, A. Soibel, Y. Myasoedov, M. Rappaport, E. Zeldov, M. Menghini, Y. Fasano, F. de la Cruz, C. J. van der Beek, M. Konczykowski, and T. Tamegai, *Phys. Rev. Lett.* **90**, 087004 (2003).
 - ¹⁶M. Menghini, Yanina Fasano, F. de la Cruz, S. S. Banerjee, Y. Myasoedov, E. Zeldov, C. J. van der Beek, M. Konczykowski, and T. Tamegai, *Phys. Rev. Lett.* **90**, 147001 (2003).
 - ¹⁷S. S. Banerjee, S. Goldberg, A. Soibel, Y. Myasoedov, M. Rappaport, E. Zeldov, F. de la Cruz, C. J. van der Beek, M. Konczykowski, T. Tamegai, and V. M. Vinokur, *Phys. Rev. Lett.* **93**, 097002 (2004).
 - ¹⁸S. Tyagi and Y. Y. Goldschmidt, *Phys. Rev. B* **67**, 214501 (2003).
 - ¹⁹C. Dasgupta and O. T. Valls, *Phys. Rev. Lett.* **91**, 127002 (2003).
 - ²⁰Y. Nonomura and X. Hu, *Europhys. Lett.* **65**, 533 (2004).
 - ²¹Y. Y. Goldschmidt and E. Cuansing, *Phys. Rev. Lett.* **95**, 177004 (2005).
 - ²²D. R. Nelson and V. M. Vinokur, *Phys. Rev. Lett.* **68**, 2398 (1992).
 - ²³L. Radzihovsky, *Phys. Rev. Lett.* **74**, 4923 (1995).
 - ²⁴C. J. van der Beek, M. Konczykowski, A. V. Samoilov, N. Chikumoto, S. Bouffard, and M. V. Feigel'man, *Phys. Rev. Lett.* **86**, 5136 (2001).
 - ²⁵A. V. Lopatin and V. M. Vinokur, *Phys. Rev. Lett.* **92**, 067008 (2004).
 - ²⁶H. Pastoriza, M. F. Goffman, A. Arribere, and F. de la Cruz, *Phys. Rev. Lett.* **72**, 2951 (1994).
 - ²⁷N. Avraham, Y. Y. Goldschmidt, J. T. Liu, Y. Myasoedov, R. Rappaport, E. Zeldov, C. J. van der Beek, M. Konczykowski, and T. Tamegai, *Phys. Rev. Lett.* **99**, 087001 (2007).
 - ²⁸D. M. Ceperley, *Rev. Mod. Phys.* **67**, 279 (1995).
 - ²⁹Y. Y. Goldschmidt, *Phys. Rev. B* **72**, 064518 (2005).
 - ³⁰Y. Y. Goldschmidt and S. Tyagi, *Phys. Rev. B* **71**, 014503 (2005).
 - ³¹S. Tyagi and Y. Y. Goldschmidt, *Phys. Rev. B* **70**, 024501 (2004).
 - ³²J. Bardeen and M. J. Stephen, *Phys. Rev.* **140**, A1197 (1965).
 - ³³L. N. Bulaevskii, J. H. Cho, M. P. Maley, P. Kes, Q. Li, M. Suenaga, and M. Ledvij, *Phys. Rev. B* **50**, R3507 (1994).
 - ³⁴L. N. Bulaevskii, M. Ledvij, and V. G. Kogan, *Phys. Rev. B* **46**, 11807 (1992).
 - ³⁵A. Buzdin and D. Feinberg, *Physica C* **235-240**, 2755 (1994).
 - ³⁶G. S. Mkrtchyan and V. V. Schmidt, *Sov. Phys. JETP* **34**, 195 (1972).
 - ³⁷S. Ryu, S. Doniach, G. Deutscher, and A. Kapitulnik, *Phys. Rev. Lett.* **68**, 710 (1992); S. Ryu, Ph.D. thesis, Stanford University, 1995.
 - ³⁸H. Nordborg and G. Blatter, *Phys. Rev. B* **58**, 14556 (1998).
 - ³⁹T. Hwa, D. R. Nelson, and V. M. Vinokur, *Phys. Rev. B* **48**, 1167 (1993).
 - ⁴⁰D. R. Nelson and V. M. Vinokur, *Phys. Rev. B* **48**, 13060 (1993).
 - ⁴¹G. Refael, W. Hofstetter, and D. R. Nelson, *Phys. Rev. B* **74**, 174520 (2006).
 - ⁴²B. Hayani, S. T. Johnson, L. Fruchter, and C. J. van der Beek, *Phys. Rev. B* **61**, 717 (2000).
 - ⁴³L. Civale, A. D. Marwick, T. K. Worthington, M. A. Kirk, J. R. Thompson, L. Krusin-Elbaum, Y. Sun, J. R. Clem, and F. Holtzberg, *Phys. Rev. Lett.* **67**, 648 (1991).
 - ⁴⁴A. Silhanek, L. Civale, S. Candia, G. Nieva, G. Pasquini, and H. Lanza, *Phys. Rev. B* **59**, 13620 (1999).
 - ⁴⁵R. J. Drost, C. J. van der Beek, J. A. Heijn, M. Konczykowski, and P. H. Kes, *Phys. Rev. B* **58**, R615 (1998).
 - ⁴⁶N. Kameda, T. Shibauchi, M. Tokunaga, S. Ooi, T. Tamegai, and M. Konczykowski, *Phys. Rev. B* **72**, 064501 (2005).
 - ⁴⁷L. N. Bulaevskii, V. M. Vinokur, and M. P. Maley, *Phys. Rev. Lett.* **77**, 936 (1996).
 - ⁴⁸A. E. Koshelev, *Phys. Rev. Lett.* **83**, 187 (1999).